

Tusas: A fully implicit parallel approach for coupled nonlinear equations

Supriyo Ghosh^{a,*}, Christopher K. Newman^a and Marianne M. Francois^b

^a*Fluid Dynamics and Solid Mechanics Group (T-3), Los Alamos National Laboratory, Los Alamos, NM 87545, USA*

^b*Theoretical Division (T-DO), Los Alamos National Laboratory, Los Alamos, NM 87545, USA*

ARTICLE INFO

Keywords:

Implicit methods
JFNK method
Preconditioning
Phase-field simulation
Solidification

ABSTRACT

We develop a fully-coupled, fully-implicit approach for phase-field modeling of solidification in metals and alloys. Predictive simulation of solidification in pure metals and metal alloys remains a significant challenge in the field of materials science, as microstructure formation during the solidification process plays a critical role in the properties and performance of the solid material. Our simulation approach consists of a finite element spatial discretization of the fully-coupled nonlinear system of partial differential equations at the microscale, which is treated implicitly in time with a preconditioned Jacobian-free Newton-Krylov method. The approach allows time steps larger than those restricted by the traditional explicit CFL limit and is algorithmically scalable as well as efficient due to an effective preconditioning strategy based on algebraic multigrid and block factorization. We implement this approach in the open-source *Tusas* framework, which is a general, flexible tool developed in C++ for solving coupled systems of nonlinear partial differential equations. The performance of our approach is analyzed in terms of algorithmic scalability and efficiency, while the computational performance of *Tusas* is presented in terms of parallel scalability and efficiency on emerging heterogeneous architectures. We demonstrate that modern algorithms, discretizations, and computational science, and heterogeneous hardware provide a robust route for predictive phase-field simulation of microstructure evolution during additive manufacturing.

1. Introduction

Microstructure evolution during the processing stage determines the properties of the final material in manufacturing applications. The key materials processes are categorized broadly as solidification and solid-state phase transformations. Solidification controls the size, shape, distribution, and morphology of the microstructure grains, and the subsequent solid-state phase transformation processes control the grain growth. Therefore, understanding of the solidification behavior of materials is essential and often regarded as a benchmark test problem for verification and validation of concerned numerical approaches. In particular, dendrite growth during solidification of metal materials is commonly studied and utilized for verification and validation of solidification models [1, 2].

Recently there has been an identified need for an improved predictive simulation capability for additive manufacturing (AM) processes [3, 4]. Improved simulation capability will allow many important AM-specific physics questions to be answered for the first time and is necessary to improve quality, decrease processing time, and eventually minimize costs of an AM product. An invaluable, individual component to this capability is the ability to simulate microstructure evolution during solidification. The phase-field approach has demonstrated particular success for microstructure evolution during the rapid solidification in metal AM processes, resulting in dendritic microstructures [5–12].

*Corresponding author. *Email address:* `supriyo.ghosh@lanl.gov` (Supriyo Ghosh) ORCID(s):

The phase-field method [13–16] is a common approach for quantitative modeling of dendrite growth. Depending on the nature of the process, the phase-field method addresses multiple variables, including composition, anisotropy, phase, temperature, orientation, and stress, fully-coupled as a set of nonlinear partial differential equations (PDEs), typically posed on high-resolution meshes. There are challenges to applying phase-field methods for predictive simulation of solidification microstructures. Three critical challenges include:

1. Ability to control restrictive time scales due to stability constraints and stiff physics.
2. Ability to control restrictive length scales and inherent large problem size due to mesh resolution necessary to resolve the diffuse interface and a large set of fully-coupled nonlinear PDEs.
3. Code flexibility required to couple a large set of arbitrary PDEs and multiphysics at run time, while effectively and efficiently leveraging modern computer architectures and software.

Many current phase-field simulation efforts utilize explicit time integration methods, which can be impractical due to constraints on the maximum stable time step due to the Courant-Friedrichs-Lewy (CFL) condition [17]. Additionally, many efforts utilize finite difference or finite volume spatial discretizations that are limited to second-order accuracy on regular, structured meshes. Furthermore, many phase-field codes are implemented using FORTRAN, which poses difficulties in utilizing modern libraries and to leverage modern architectures effectively.

Our approach to phase-field modeling particularly addresses the above challenges. We mitigate time scale challenges by utilizing implicit temporal integration, which allows time steps much larger than the explicit CFL limit and readily affords second-order and higher time integration. A direct advantage of implicit methods is that relatively large, second-order time steps can be taken, since the time step is determined by accuracy instead of by numerical stability constraints. A disadvantage, however, is that fully implicit methods require a nonlinear solution be attained for each time step.

Additionally, we utilize finite element spatial discretization methods [18, 19] for mitigation of length scale challenges. The finite element method allows second-order and third-order approximations on unstructured meshes, and is easily implemented in three-dimensions (3D), and is particularly suited for simulation of complex geometries such as solidification melt pools in AM processes.

In recent years, there has been considerable advancement in both linear and nonlinear solution methods. Recent developments in Jacobian-free Newton-Krylov (JFNK) methods [20, 21], physics-based preconditioning [22], and efficient linear solvers, such as GMRES [23], have allowed efficient solution of coupled nonlinear problems and effective fully implicit time integration. These algorithms, combined with modern software and libraries, provide a robust route to flexible multiphysics simulations on modern, emerging heterogeneous supercomputer architectures.

The phase-field approach is computationally intensive; a high computational cost is required to resolve scientifically relevant length and time scales associated with microstructure patterns that result due to phase change, species diffusion, and heat flow during solidification. To accurately simulate such multiphysics phenomena, it is often necessary to perform large-scale simulations at small time steps, requiring many hours or days of conventional computational resources. Parallel computing approaches *via* distributed memory Message Passing Interface (MPI) [24], shared memory OpenMP [25], and Compute Unified Device Architecture (CUDA) for Graphics Processing Units (GPUs) [26] are currently being utilized to attain computational performance and parallel scalability. Recently, hybrid approaches *via* MPI+OpenMP, for CPU-parallel architectures, or MPI+CUDA, for CPU/GPU architectures, have been adopted to further speed up the simulations in a variety of applications [27–29]. The advantages of hybrid MPI+CUDA based parallel computing in which both massive computational power and wide memory bandwidth will allow large-scale phase-field simulations to achieve superior performance and parallel scalability.

Software development for phase-field simulation is an emerging need for multiphysics materials modeling capability. Existing software within the phase-field community include MOOSE [30],

PACE3D [31], MMSP [32], MICRESS [33], OpenPhase [34], PhasePot [35], FiPy [36], PRISMS-PF [37], AMPE [38], and MEUMAPPS [39]. These frameworks, each containing phase-field models targeted for different applications with different sets of coupled nonlinear PDEs, are implemented with various discretizations and algorithmic approaches. To date, the majority of these efforts are based on finite difference spatial discretization or explicit time integration. Some frameworks such as MOOSE [30] and PACE3D [31] are implemented in 3D on conventional CPU-parallel architectures; however, these codes are not known to scale and do not make use of next-generation heterogeneous CPU/GPU architectures necessary to accelerate computational performance required for materials simulation and development. Currently, there are only a few computational efforts on phase-field methods implemented within hybrid CPU/GPU architectures [40–42]. However, these are single-purpose codes, with numerical approaches limited only to specific phase-field implementations and thus can not be easily generalized to incorporate additional multiphysics modules.

In this work, we implement phase-field methods for solidification within the Tusas software environment. Tusas is a general, flexible code for solving coupled systems of nonlinear PDEs and was originally developed particularly for phase-field simulation of solidification. The Tusas approach consists of a finite element spatial discretization of the fully-coupled nonlinear system, which is treated explicitly or implicitly in time with a preconditioned JFNK method. In addition, Tusas leverages modern computational science and state-of-the-art software libraries that enable scalable and efficient predictive simulation of microstructure evolution on heterogeneous architectures.

This manuscript is organized as follows: a description of the phase-field equations, finite element and temporal discretizations, and solution strategies are presented in Sec. 2; an overview of Tusas is outlined in Sec. 3; results in terms of accuracy, algorithmic efficiency, and parallel performance for two academic problems: solidification of homogeneous materials and solidification of dilute binary alloys, in addition to a comparison to explicit temporal methods, are presented in Sec. 4; conclusions are drawn in Sec. 5.

2. Mathematical approach

The phase-field method [13–16] is a powerful technique utilized to simulate microstructure evolution during solidification. A particular strength of the method is that the sharp solid-liquid interface is modeled by a well-localized, but diffuse interface with a finite width; which reduces to a set of nonlinear PDEs that are handled by standard numerical techniques. As we do not seek to detail the phase-field technique here, we only describe the model equations to convey the numerical schemes adopted in Tusas.

2.1. Problem description: Phase-field technique

Let the scalar variable phase-field $\varphi(\mathbf{x}, t)$, solute concentration $u(\mathbf{x}, t)$, and temperature $T(\mathbf{x}, t)$, describe the non-equilibrium dynamics of a material undergoing the solidification process, resulting in microstructure patterns. The variable φ describes the physical state of the microstructure regions. While the bulk phases, solid and liquid, are represented by constant values of φ , the solid-liquid interface is identified by continuous transition of φ between bulk phases. With this description, the interface is not tracked explicitly but is given implicitly by a contour of φ , making the implementation relatively straightforward compared to sharp-interface methods [43, 44] and easily extendable to 3D. Let the material occupy a spatial region $\Omega \subset \mathbb{R}^3$ with boundary $\partial\Omega$, with $\mathbf{x}(\in \Omega) = [x \ y \ z]^T$ is the spatial variable, and $t \in [0, \infty)$ is time. The material is described by the Helmholtz free energy functional [13–16],

$$\mathcal{F} = \int_{\Omega} \left[f(\varphi, u, T) + \frac{\sigma^2}{2} |\nabla \varphi|^2 \right] d\mathbf{x}, \quad (1)$$

where $f(\varphi, u, T)$ is the bulk free energy, and the second term is the interface free energy in which the coefficient σ^2 relates to the width of the diffuse interface. Although Eq. (1) is the starting point for most phase-field models, there can be additional terms due to the coupling of the field variables and contributions from driving forces during the materials process, see [13–16]. The minimization of the functional \mathcal{F} with respect to field variables [45, 46] yields the following PDEs for temporal evolution of field variables,

$$\varphi_t + \frac{1}{\tau} \frac{\delta \mathcal{F}}{\delta \varphi} = \varphi_t + \frac{1}{\tau} \left(\frac{\partial f}{\partial \varphi} - \sigma^2 \nabla \cdot \nabla \varphi \right) = 0, \quad (2)$$

$$u_t - \nabla \cdot \left(D \nabla \frac{\delta \mathcal{F}}{\delta u} \right) = u_t - \nabla \cdot \left(D \nabla \frac{\partial f}{\partial u} \right) = 0, \quad (3)$$

and

$$T_t - \alpha \nabla \cdot \nabla T - G_1 = 0. \quad (4)$$

Here, the subscript t denotes partial differentiation with respect to t , $\nabla \cdot$ and ∇ are the divergence and gradient operators, τ is the time scale related to atomic mobility at the interface, and D is the diffusivity related to mobility of solute in the liquid. Equation (2) is the Allen-Cahn equation [47] for the non-conserved variable φ , Eq. (3) is the Cahn-Hilliard diffusion equation [48] for the conserved field u , and Eq. (4) is a standard thermal diffusion equation with thermal diffusivity α and heat source term for solidification $G_1 = L/c_p \varphi_t$, where L is the latent heat and c_p the specific heat. For the example problems in this manuscript, we employ zero Neumann boundary conditions on $\partial\Omega$ and specify initial conditions for $\varphi(\mathbf{x}, 0)$, $u(\mathbf{x}, 0)$, and $T(\mathbf{x}, 0)$.

2.1.1. Finite element formulation

We utilize the weak form of Eqs. (2)–(4) and choose an appropriate subspace of $V \subset H^1(\Omega)$ approximated by V_h , where V_h is a Lagrange (nodal) finite element spatial discretization such that $V_h \subset V$ and $V_h = \text{span}\{\psi_j(\mathbf{x})\}_{j=1}^E$. Here, h is a discretization parameter chosen as a measure of the mesh size, and E is the number of nodes in the mesh. Let $\varphi_h = \sum_{j=1}^E \varphi_j(t) \psi_j(\mathbf{x})$, $u_h = \sum_{j=1}^E u_j(t) \psi_j(\mathbf{x})$, and $T_h = \sum_{j=1}^E T_j(t) \psi_j(\mathbf{x})$ be the discretizations in $V \times [0, \infty)$ of φ , u , and T , respectively. The finite element form of Eqs. (2)–(4) is given by:

$$(\varphi_{ht}, \psi_i) + \left(\frac{1}{\tau} \frac{\partial f}{\partial \varphi_h}, \psi_i \right) + (\sigma^2 \nabla \varphi_h, \nabla \psi_i) = 0, \quad (5)$$

$$(u_{ht}, \psi_i) + \left(D \nabla \frac{\partial f}{\partial u_h}, \nabla \psi_i \right) = 0, \quad (6)$$

and

$$(T_{ht}, \psi_i) + (\alpha \nabla T_h, \nabla \psi_i) - (G_1, \psi_i) = 0, \quad (7)$$

for all $\psi_i \in V_h$, where $(\varphi, \psi) = \int_{\Omega} \varphi \cdot \psi \, d\Omega$ depicts the inner product in $L^2(\Omega)$, and we have applied Green's theorem [19]. For the example problems in this manuscript, we approximate V_h using bilinear quadrilateral (Q1) or biquadratic quadrilateral (Q2) element spaces in 2D and bilinear hexahedral element spaces in 3D [18, 19].

2.1.2. Time integration

We discretize Eqs. (5)–(7) temporally with a weighted method and define the residual $\mathbf{F} = [F_1 \ F_2 \ F_3]^\top$ as follows:

$$F_1(\varphi_h^{n+1}, u_h^{n+1}, T_h^{n+1})_i := \frac{1}{\Delta t} (\varphi_h^{n+1} - \varphi_h^n, \psi_i) + \theta \left(\left(\frac{1}{\tau} \frac{\partial f}{\partial \varphi} \right)^{n+1}, \psi_i \right) + (1-\theta) \left(\left(\frac{1}{\tau} \frac{\partial f}{\partial \varphi} \right)^n, \psi_i \right) \\ + \theta (\sigma^2 \nabla \varphi_h^{n+1}, \nabla \psi_i) + (1-\theta) (\sigma^2 \nabla \varphi_h^n, \nabla \psi_i), \quad (8)$$

$$F_2(\varphi_h^{n+1}, u_h^{n+1}, T_h^{n+1})_i := \frac{1}{\Delta t} (u_h^{n+1} - u_h^n, \psi_i) + \theta \left(\left(D \nabla \frac{\partial f}{\partial u} \right)^{n+1}, \nabla \psi_i \right) \\ + (1-\theta) \left(\left(D \nabla \frac{\partial f}{\partial u} \right)^n, \nabla \psi_i \right), \quad (9)$$

and

$$F_3(\varphi_h^{n+1}, u_h^{n+1}, T_h^{n+1})_i := \frac{1}{\Delta t} (T_h^{n+1} - T_h^n, \psi_i) + \theta (\alpha \nabla T_h^{n+1}, \nabla \psi_i) \\ + (1-\theta) (\alpha \nabla T_h^n, \nabla \psi_i) - \left(G_1(\widehat{\varphi}_h^n), \psi_i \right), \quad (10)$$

with

$$\widehat{\varphi}_h^n = \frac{\theta}{\Delta t} (\varphi_h^{n+1} - \varphi_h^n) + \frac{1-\theta}{\Delta t} (\varphi_h^n - \varphi_h^{n-1}). \quad (11)$$

We use superscripts to denote time index, $\Delta t = t^{n+1} - t^n$, which is uniform time step size from time n to time $n+1$, $\theta = 0$ corresponds to the explicit (forward) Euler method, $\theta = 1$ corresponds to the implicit (backward) Euler method, and $\theta = 1/2$ corresponds to the implicit trapezoidal method (often referred to as Crank-Nicolson) [17]. The subscript i refers to vector index. To determine φ_i^{n+1} , u_i^{n+1} and T_i^{n+1} , we solve a fully-coupled, nonlinear system of

$$\mathbf{F}(\mathbf{U}) = 0, \quad (12)$$

with

$$\mathbf{F}(\mathbf{U}) = [F_1 \ F_2 \ F_3]^\top \quad (13)$$

and

$$\mathbf{U}_i = [\varphi_i^{n+1} \ u_i^{n+1} \ T_i^{n+1}]^\top, \quad (14)$$

at each time step. Our approach is to approximate a solution to Eq. (12) with a Jacobian-free Newton-Krylov method discussed in Sec. 2.2.

2.2. Jacobian-free Newton-Krylov (JFNK) methods

We briefly describe the JFNK method. More detailed analyses can be found in [20, 21]. The JFNK method for the discrete problem is

$$\mathbf{F}(\mathbf{U}) = \mathbf{0}, \quad (15)$$

with $\mathbf{F} : \mathbb{R}^N \rightarrow \mathbb{R}^N$, where N is the number of unknowns. Given the Jacobian, $\mathbf{F}'(\mathbf{U})$, with $\mathbf{F}'(\mathbf{U})_{ij} = \partial \mathbf{F}(\mathbf{U})_i / \partial \mathbf{U}_j$, it is straightforward to express the Newton iteration,

$$\mathbf{F}'(\mathbf{U}^{(l)}) \delta \mathbf{U}^{(l)} = -\mathbf{F}(\mathbf{U}^{(l)}) \quad (16)$$

and

$$\mathbf{U}^{(l+1)} \leftarrow \mathbf{U}^{(l)} + \Lambda \delta \mathbf{U}^{(l)}, \quad (17)$$

where the superscript (l) denotes the iteration count of the Newton iteration, and $\delta \mathbf{U}^{(l)} = \mathbf{U}^{(l+1)} - \mathbf{U}^{(l)}$ is the Newton step. The step length, $\Lambda \in (0, 1]$, is chosen by a backtracking line search strategy, such that

$$\|\mathbf{F}(\mathbf{U}^{(l)} + \Lambda \delta \mathbf{U}^{(l)})\|_2 \leq \|\mathbf{F}(\mathbf{U}^{(l)})\|_2. \quad (18)$$

Typically, Λ is initially chosen as $\Lambda = 1$ and is reduced until Eq. (18) is satisfied. This process is also known as globalization [49, 50]. The Newton iteration is terminated when

$$\|\mathbf{F}(\mathbf{U}^{(l)})\|_2 < \tau_r \|\mathbf{F}(\mathbf{U}^{(0)})\|_2 + \tau_a, \quad (19)$$

where τ_r is a specified relative tolerance, τ_a is a specified absolute tolerance, and $\|\cdot\|_2$ is the Euclidean norm on l^2 .

Newton's method is impractical for solving large systems due to the high computational cost associated with forming the Jacobian $\mathbf{F}'(\mathbf{U})$. Therefore, Krylov iterative solvers such as generalized minimum residual (GMRES) algorithm [23] are used to solve the linear system in Eq. (16). This approach does not require the Jacobian matrix itself, but utilizes the operation of the Jacobian matrix on a vector \mathbf{v} . Approximating this matrix-vector product by a finite difference is the basis of the JFNK method. Specifically, to evaluate the matrix-vector product $\mathbf{F}'(\mathbf{U}^{(l)})\mathbf{v}$, a finite-difference approach,

$$\mathbf{F}'(\mathbf{U}^{(l)})\mathbf{v} \approx \frac{1}{\varepsilon} (\mathbf{F}(\mathbf{U}^{(l)} + \varepsilon \mathbf{v}) - \mathbf{F}(\mathbf{U}^{(l)})), \quad (20)$$

is commonly used [20, 51], where ε is chosen heuristically to avoid problems with machine precision [52]. As $\mathbf{F}(\mathbf{U}^{(l)})$ is readily available in the JFNK method, each GMRES iteration only requires an evaluation of $\mathbf{F}(\mathbf{U}^{(l)} + \varepsilon \mathbf{v})$.

An inexact convergence tolerance is used on the linear solve for the JFNK method [51, 53, 54]. The tolerance to which we solve the linear problem on each nonlinear iteration is related to the current nonlinear residual, $\mathbf{F}(\mathbf{U}^{(l)})$, by

$$\|\mathbf{F}'(\mathbf{U}^{(l)}) \delta \mathbf{U}^{(l)} + \mathbf{F}(\mathbf{U}^{(l)})\|_2 \leq \eta_{(l)} \|\mathbf{F}(\mathbf{U}^{(l)})\|_2, \quad (21)$$

with

$$\eta_{(l)} = \gamma \left(\frac{\|\mathbf{F}(\mathbf{U}^{(l)})\|_2}{\|\mathbf{F}(\mathbf{U}^{(l-1)})\|_2} \right)^\omega \quad (22)$$

and

$$\max(\gamma \eta_{(l-1)}^\omega, \eta_{\min}) \leq \eta_{(l)} \leq \eta_{\max}. \quad (23)$$

Equations (21)–(23) are commonly referred to as the forcing term, and its particular choice is critical to efficiency of the JFNK method. Our choice of values for γ , ω , $\eta_{(0)}$, η_{\min} and η_{\max} are provided in Sec. 4.1.

2.3. Preconditioning

The dominant cost of the JFNK method is GMRES iteration. To reduce the number of GMRES iterations, preconditioning is used. We apply physics-based preconditioning [22, 55] as a right preconditioning process \mathbf{M}^{-1} , and the matrix-vector product expression in Eq. (20) becomes

$$\mathbf{F}'(\mathbf{U}^{(l)})\mathbf{M}^{-1}\mathbf{v} \approx \frac{1}{\varepsilon} (\mathbf{F}(\mathbf{U}^{(l)} + \varepsilon\mathbf{M}^{-1}\mathbf{v}) - \mathbf{F}(\mathbf{U}^{(l)})). \quad (24)$$

The operator \mathbf{M}^{-1} is chosen such that $\mathbf{M}^{-1}\mathbf{v}$ is a suitable approximation to $\mathbf{F}'(\mathbf{U}^{(l)})^{-1}\mathbf{v}$. In addition, $\mathbf{M}^{-1}\mathbf{v}$ should be inexpensive to construct and apply.

We introduce a process for applying the preconditioner. As Eqs. (5)–(7) constitute a parabolic system of PDEs, we address dominant time scales that are important for constructing our preconditioner and examine a linearized form of the Jacobian to arrive at the preconditioning operator \mathbf{M}^{-1} .

2.3.1. Time scales

The time scales associated with diffusion in Eqs. (5)–(7) are given by:

$$\Delta t_\varphi \leq C_\varphi \tau h^2 / \sigma^2, \quad (25)$$

$$\Delta t_u \leq C_u h^2 / D, \quad (26)$$

and

$$\Delta t_T \leq C_T h^2 / \alpha, \quad (27)$$

respectively; where h is associated with mesh size and C_φ , C_u , and C_T are constants independent of h . Equations (25)–(27) determine the maximum stable time step for explicit methods [17] applied to Eqs. (8)–(10). In typical material processes, $\Delta t_\varphi > \Delta t_u > \Delta t_T$ is valid [56].

The separation between these time scales presents challenges for time integration. We call a time integration method *algorithmically scalable* if the CPU time is inversely proportional to the time step size. Explicit time integration to a fixed computation time is inherently algorithmically scalable; if the time step size is doubled, CPU time is reduced by a half. A drawback of explicit methods is the stability restriction of the maximum time step size. Explicit methods for phase-field simulations are unstable for time steps larger than Δt_T . While implicit methods have superior stability properties, when applied to problems with nonlinear diffusion, conditioning of the linear system typically suffers when $\Delta t > \Delta t_T$, requiring many linear iterations for convergence of the linear solver. This is particularly true for Eqs. (8)–(10). Hence, implicit time integration methods, in general, do not scale well algorithmically unless effectively preconditioned.

Our goal is to integrate the fully-coupled system of Eqs. (8)–(10) with an implicit time integration with time steps $\Delta t > \Delta t_\varphi$ (Eq. (25)) that are larger than the explicit time step limit Δt_T , while maintaining the second-order accuracy and algorithmic scalability.

2.3.2. Construction of preconditioner

We construct a preconditioning operator, \mathbf{M}^{-1} , that is effective when $\Delta t > \Delta t_T$. Recall that \mathbf{M}^{-1} has the properties that $\mathbf{M}^{-1}\mathbf{v}$ is a suitable approximation to $\mathbf{F}'(\mathbf{U}^{(l)})^{-1}\mathbf{v}$, and $\mathbf{M}^{-1}\mathbf{v}$ should be inexpensive to construct and apply. We drop superscripts and consider the Jacobian of Eqs. (8)–(10),

$$\mathbf{F}'(\mathbf{U}) = \begin{bmatrix} \frac{\partial F_1(\varphi, u, T)}{\partial \varphi} & \frac{\partial F_1(\varphi, u, T)}{\partial u} & \frac{\partial F_1(\varphi, u, T)}{\partial T} \\ \frac{\partial F_2(\varphi, u, T)}{\partial \varphi} & \frac{\partial F_2(\varphi, u, T)}{\partial u} & \frac{\partial F_2(\varphi, u, T)}{\partial T} \\ \frac{\partial F_3(\varphi, u, T)}{\partial \varphi} & \frac{\partial F_3(\varphi, u, T)}{\partial u} & \frac{\partial F_3(\varphi, u, T)}{\partial T} \end{bmatrix} := \begin{bmatrix} M_{11} & M_{12} & M_{13} \\ M_{21} & M_{22} & M_{23} \\ M_{31} & M_{32} & M_{33} \end{bmatrix}, \quad (28)$$

and construct \mathbf{M} as an approximation to $\mathbf{F}'(\mathbf{U})$ by discarding off-diagonal blocks to arrive at

$$\mathbf{M} = \text{diag}(M_{11}, M_{22}, M_{33}). \quad (29)$$

By ignoring off-diagonal terms, we have accepted that our preconditioner will be less effective when the solver uses time steps approaching small time scales. Note that inversion of Eq. (29) is equivalent to one iteration of the block-Jacobi method [21]. In our examples, the matrix in Eq. (29) is approximately inverted blockwise using algebraic multigrid methods [57–59]. In particular, we utilize the ML [60] and MueLu [61, 62] packages within the Trilinos library [63, 64].

3. Tusas

To mitigate the challenges due to time scales, length scales, and their coupling, we have designed Tusas with the following advanced capabilities:

- *Higher-order discretization methods:* Tusas utilizes an unstructured finite element spatial discretization, which can be more flexible and functional for arbitrary mesh geometries compared to finite difference or finite volume methods [18, 19]. Discretizations consist of linear and bilinear quadrilateral, triangular, tetrahedral, or hexahedral Lagrange (nodal) elements in 2D and 3D. Meshing is facilitated through the Exodus II library [65, 66]. Time integration techniques implemented in Tusas include explicit and implicit Euler, Crank-Nicolson, general second-order backward difference formula, and methods based on implicit midpoint rule. Implicit methods possess less restrictive time step stability requirements, allowing for larger time steps than explicit methods; and, as we show in Sec. 4.1.2, can provide less computational cost for a given level of accuracy than explicit methods.
- *Robust algorithms and solvers:* Tusas leverages the Trilinos library [64] and utilizes JFNK nonlinear solvers provided by NOX [67] and GMRES linear solvers provided by Belos [68] and AztecOO [69]. The key to an efficient implementation of JFNK is effective preconditioning. As the dominant cost of JFNK is the linear solver, Eq. (16), effective preconditioning reduces the number of linear solver iterations per Newton iteration. Our preconditioning strategy is based on block factorization and algebraic multigrid (AMG) methods using the ML [60] and MueLu [61, 62] libraries. We show specifically in Sec. 4.1.2 that the use of these packages and algorithms allow for efficient implicit time integration while affording algorithmic scalability.
- *Modular object-oriented programming:* The combination of finite element discretization and JFNK allows for a unique opportunity to leverage modular, object-oriented software development. The JFNK method only requires evaluation of the residual, Eqs. (5)–(7), realized on each element *via* pointwise evaluation at Gauss points. Hence, from an implementation standpoint, Tusas allows a flexible framework as it only requires the user to implement code for each block of the residual equation, independent of dimension, and supports a variety of easily coupled phase-field models. Optionally, Tusas allows the user to implement code for each block row of the preconditioning matrix, Eq. (29). Tusas is written in C++ and provides a flexible interface that enables runtime configuration and coupling of a large set of arbitrary PDEs and complex multiphysics at run time. Since it is impractical to implement new code every time a set of similar or additional physics is required to solve, the Tusas framework leverages the modern polymorphic features of C++ to enable effective code reusability, allowing rapid development of the code without requiring extensive modification. The inherent flexibility of the Tusas framework additionally allows runtime problem configuration *via* C++ function containers. In addition to Trilinos, Tusas makes heavy utilization of CMake [70], Boost [71], HDF5 [72], and NetCDF [73].

- *Massively parallel computing*: Tusas is designed to leverage hierarchical parallelism on emerging heterogeneous hardware and architectures. In particular, Tusas utilizes the Trilinos Kokkos library [74, 75]. Kokkos provides an abstract interface for shared memory to both the OpenMP library [25] for threading on CPU hardware, and the Cuda library [26] for execution on GPU hardware. Execution on multi-node, distributed memory hardware for multi-CPU and multi-GPU execution is afforded by MPI [24]. As we are designing high-fidelity microstructure simulations, we are observing an increasing need for exascale computing (one quintillion (10^{18}) floating-point operations per second). By utilizing MPI and Kokkos, Tusas is uniquely targeted to emerging exascale architectures. We demonstrate the ability of Tusas to scale both strongly and weakly with up to 1 billion unknowns on thousands of GPUs in Sec. 4.3.

We refer the reader to the GitHub page (<https://github.com/chrisknewman/tusas>) [76] for instructions on how to obtain, install, compile, and execute Tusas.

4. Results

To demonstrate the performance and flexibility of Tusas framework, we examine two examples from phase-field simulation of solidification. The first example is free dendrite growth in a homogeneous pure metal melt. In this example, we focus on algorithmic performance, specifically in terms of accuracy and efficiency. The second example is columnar dendrite growth during directional solidification of a dilute binary metal alloy; here, we examine parallel scalability and efficiency of 3D simulations on emerging supercomputer architectures.

4.1. Free growth

Dendritic solidification in a homogeneous material (in the absence of concentration) is well-understood community-determined reference benchmark problem to validate phase-field frameworks [37, 77]. To model this test problem, we adopt the mathematical forms of the nonlinear equations for φ and T given in [78]. Applying non-dimensionalization with a particular choice of $f(\varphi, T)$, Eq. (8) becomes

$$\begin{aligned}
F_1(\varphi_h^{n+1}, T_h^{n+1})_i &= \frac{1}{\Delta t} (g_s^2(\vartheta^{n+1})\varphi_h^{n+1} - g_s^2(\vartheta^n)\varphi_h^n, \psi_i) \\
&+ \theta \beta \Gamma (g_s^2(\vartheta^{n+1})\nabla\varphi_h^{n+1}, \nabla\psi_i) + (1 - \theta) \beta \Gamma (g_s^2(\vartheta^n)\nabla\varphi_h^n, \nabla\psi_i) \\
&+ \frac{\theta}{2} \left(\|\nabla\varphi_h^{n+1}\| \|\nabla_{\nabla\varphi_h} g_s^2(\vartheta^{n+1}), \nabla\psi_i \right) + \frac{1 - \theta}{2} \left(\|\nabla\varphi_h^n\| \|\nabla_{\nabla\varphi_h} g_s^2(\vartheta^n), \nabla\psi_i \right) \\
&+ \theta (G_2(\varphi_h^{n+1}, T_h^{n+1}), \psi_i) + (1 - \theta) (G_1(\varphi_h^n, T_h^n), \psi_i), \quad (30)
\end{aligned}$$

with

$$G_2(\varphi_h, T_h) = \beta \Gamma \frac{\varphi_h(1 - \varphi_h)(1 - 2\varphi_h)}{h^2} - 5 \beta (T_m - T_h) \frac{\varphi_h^2(1 - \varphi_h)^2}{h}, \quad (31)$$

and the operator

$$\nabla_{\nabla\varphi} = \left[\frac{\partial}{\partial\varphi_x} \quad \frac{\partial}{\partial\varphi_y} \quad \frac{\partial}{\partial\varphi_z} \right]^T. \quad (32)$$

Here,

$$\sigma = g_s(\vartheta) = 1 - 3\epsilon + 4\epsilon \frac{\varphi_x^4 + \varphi_y^4 + \varphi_z^4}{\|\varphi\|^4} \quad (33)$$

ϵ	Anisotropy	0.005	Ω	Domain	$[0, 4.5] \times [0, 4.5]$
α	Thermal diffusivity	4.0	L/c_p	Latent heat	1.0
β	Kinetic coefficient	$1/\Gamma = 191.82$	T_∞	Liquidus temperature	1.0
W	Interface width	$h/0.4 = 0.02652$	Δ	Undercooling	$(T_m - T_\infty)/(L/c_p) = .55$
d_0	Capillary length	.139 W			

Table 1

Nondimensional material properties and simulation parameters in Eqs. (30)–(34), adopted from [78].

is the four-fold solid-liquid interface anisotropy with magnitude ϵ . Similarly, the dimensionless form of Eq. (10) for T becomes

$$F_3(\varphi_h^{n+1}, T_h^{n+1})_i = \frac{1}{\Delta t} (T_h^{n+1} - T_h^n, \psi_i) + \theta (\alpha \nabla T_h^{n+1}, \nabla \psi_i) + (1 - \theta) (\alpha \nabla T_h^n, \nabla \psi_i) - (G_1(\widehat{\varphi}_h^n), \psi_i). \quad (34)$$

We utilize 9 quadrature points in each quadrilateral element to accurately integrate the nonlinear terms in Eqs. (30)–(34). Initial conditions consist of a perturbed circular seed given by:

$$\varphi(\mathbf{x}, 0) = \begin{cases} 1 & : \|\mathbf{x}\| \leq r \\ 0 & : \|\mathbf{x}\| > r \end{cases}, \quad (35)$$

with radius $r = 0.3 g_s(\vartheta)$ and $T(\mathbf{x}, 0) = T_m$. We recall that $\varphi = 1$ corresponds to solid and $\varphi = 0$ corresponds to liquid. The dimensionless material parameters utilized for simulations are listed in Table 1. In this model, the length scale is d_0 and the time scale is $\tau = d_0^2/\alpha$.

Simulations were performed on $\Omega = [0, 4.5]^2$ consisting of a structured mesh with 300×300 quadrilateral elements with mesh spacing $h = 0.03$. To study convergence and algorithmic performance, we compare explicit-Euler ($\theta = 0$) and implicit Crank-Nicolson ($\theta = 1/2$) methods, with Δt varied between 10^{-3} and 10^{-6} . In addition, we compare the effects of bilinear (Q1) and biquadratic (Q2) discretizations on anisotropy. We utilize the following nonlinear solver parameters: $\eta_0 = 0.1$, $\eta_{\min} = 10^{-6}$, $\eta_{\max} = 0.01$, $\omega = 1.5$, $\gamma = 0.9$, $\tau_a = 0$, and $\tau_r = 10^{-6}$ for all simulations (Sec. 2.2).

Simulations were carried out to dimensionless time $t_f = 0.14$, far beyond dendrite tip reaching steady-state velocity, thus allowing a direct comparison with the analytical sharp-interface steady-state solutions for verification. Note that the number of time steps required to attain $t_f = 0.14$ would be different for different temporal approaches used in our simulations, since different values of Δt are required for these approaches due to CFL constraints (Sec. 2.3.1). The initial solid grows to the typical dendrite shape in Fig. 1. In particular, the initial condition, $\varphi(\mathbf{x}, 0)$, is shown in Fig. 1a and is enlarged in Fig. 1b to illustrate the background finite element mesh. Figure 1c shows the steady-state solution of φ , and steady-state T is shown in Fig. 1d.

4.1.1. Verification and validation

It is essential to perform convergence tests of the TusaS solutions to verify the temporal and spatial discretizations and to further verify with the available physics-based model analytical predictions. To demonstrate temporal convergence, we define error for $\mathbf{U}_i = [\varphi_i \ T_i]^T$ as $\|\mathbf{U} - \mathbf{U}_{\text{ref}}\|_2$, where \mathbf{U}_{ref} is a reference solution computed with the Crank-Nicolson method with $\Delta t_{\text{ref}} = 1.953125 \times 10^{-6}$. This value of Δt_{ref} was chosen such that a sufficiently high-resolution reference solution could be used for a verification of second-order convergence for the Crank-Nicolson method and first-order convergence of the explicit Euler method.

Figure 2 shows error as a function of the time step size at $t = t_f$ for explicit-Euler (EE) and implicit Crank-Nicolson (CN) methods, with Ω spatially discretized with 22,500 bilinear Lagrange (Q1) finite elements. Figure 2 also provides a verification of order-of-accuracy for each method. In particular, the

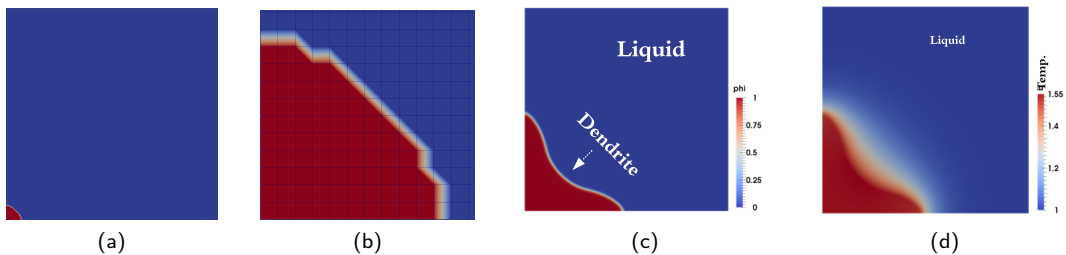


Figure 1: (a) Initial condition. (b) An enlarged view of the circular seed in a background finite element mesh. (c) Visualization of the final phase-field solution φ at the steady-state. (d) Visualization of the temperature field T at the steady-state.

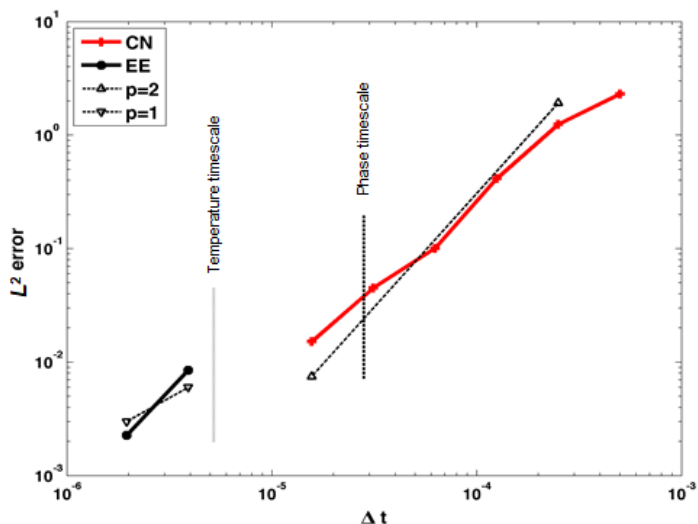


Figure 2: Verification of temporal convergence rates for Crank-Nicolson (CN) and explicit Euler (EE). Reference lines for second-order ($p = 2$) and first-order ($p = 1$) convergence and reference lines for $\Delta t = \Delta t_T$ (Temperature timescale) and $\Delta t = \Delta t_\varphi$ (Phase timescale) are shown.

EE method is first-order accurate with time step size restricted by the CFL condition associated with thermal diffusion $\Delta t < \Delta t_T$ (Eq. (27)). In contrast, the implicit CN method is second-order accurate, and allows time steps much larger than the CFL condition associated with phase diffusion $\Delta t > \Delta t_\varphi$ (Eq. (25)).

To demonstrate spatial convergence, we make use of an analytic Green's function solution for our problem; this is valid at steady-state [79] and provides a steady-state tip velocity as a function of undercooling Δ and capillary length d_0 . We use this analytical solution to make a quantitative comparison with our Crank-Nicolson solution at $t = t_f$ and $\Delta t = \Delta t_{\text{ref}}$, utilizing both bilinear (Q1) and biquadratic (Q2) Lagrange spatial discretizations with $\Delta = .55$, $d_0 = .277$, and 22, 500 finite elements. In particular, Table 2 reports our simulated dimensionless steady-state tip velocity, $\tilde{v} = v d_0 / \alpha$, the dimensionless steady-state tip velocity given by the Green's function solution, $\tilde{v}_{\text{GF}} = v_{\text{GF}} d_0 / \alpha$, the absolute error, defined as $|\tilde{v} - \tilde{v}_{\text{GF}}|$, and relative error (%), defined as $\frac{|\tilde{v} - \tilde{v}_{\text{GF}}|}{\tilde{v}_{\text{GF}}} \times 100$, for both Q1 and Q2 discretizations. The last column of Table 2 confirms the error decreases by a factor of more than

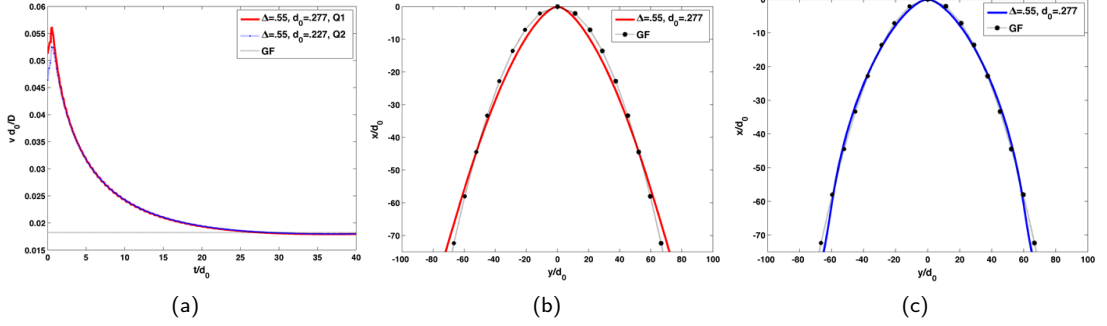


Figure 3: (a) Evolution of dimensionless dendrite tip velocity, \tilde{v} , as a function of time for Q1 and Q2 elements with undercooling $\Delta = .55$ and capillary length $d_0 = .227$; evolution of dimensionless tip velocity \tilde{v}_{GF} given by Green's function (GF). (b) Steady-state tip radius with Q1 element; tip radius given by GF. (c) Steady-state tip radius with Q2 element and GF.

Element	\tilde{v}	\tilde{v}_{GF}	$ \tilde{v} - \tilde{v}_{GF} $	Relative error
Q1	.01822	.017	.00122	7%
Q2	.01754	.017	.00054	3%

Table 2

Dimensionless steady-state dendrite tip velocities, \tilde{v} and \tilde{v}_{GF} , and error metrics for both Q1 and Q2 discretizations.

2 for Q2 compared to Q1. We note that the relative error in our calculations is similar or lower to that with other phase-field simulation frameworks for the same dendrite growth benchmark problem [37]. The evolution of tip velocity for both Q1 and Q2 is shown in Fig. 3a, which confirms that \tilde{v} reaches a fixed value upon the dendrite reaching the steady-state and shows qualitatively similar tip velocity evolution for both Q1 and Q2. Additionally, the Green's function solution provides a steady-state tip radius profile, which we use to qualitatively validate the Q1 and Q2 solutions. Figure 3b shows dimensionless steady-state tip radius for the Q1 solution and the Green's function solution; Fig. 3c shows the corresponding comparison for Q2. From a qualitative standpoint, the Q2 solution appears to more accurately resolve the Green's function solution and suggests that the higher-order biquadratic finite element may more accurately approximate the highly nonlinear anisotropic term $g_s(\vartheta)$ (Eq. (33)).

4.1.2. Algorithmic performance

We precondition JFNK with the following forms of

$$(M_{11})_{ij} = \frac{1}{\Delta t} (g_s^2(\vartheta_j) \psi_j, \psi_i) + \theta \beta \Gamma (g_s^2(\vartheta_j) \nabla \psi_j, \nabla \psi_i) \quad (36)$$

and

$$(M_{33})_{ij} = \frac{1}{\Delta t} (\psi_j, \psi_i) + \theta (\alpha \nabla \psi_j, \nabla \psi_i) \quad (37)$$

in Eq. (29) (with $(M_{22})_{ij}$ absent). For our examples, we utilize Trilinos ML [60] smoothed-aggregation multigrid approach with 2 sweeps of symmetric Gauss-Siedel error smoother, 2 V-cycles, 4 levels of coarsening, and 45,602 unknowns. Results were obtained in serial on MacBook Pro, OS X 10.9.4, 2.8 GHz Intel Core i7, 16 GB 1600 MHz DDR3, GCC 4.9.1.

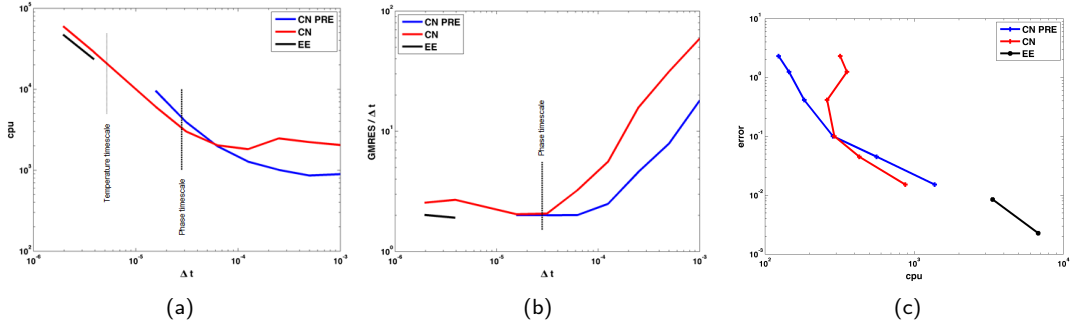


Figure 4: (a) Cost in terms of CPU time as a function of time step size for explicit Euler (EE), Crank-Nicolson (CN) and Crank-Nicolson with preconditioning (CN-PRE) and reference lines for $\Delta t = \Delta t_T$ (Temperature timescale) and $\Delta t = \Delta t_\varphi$ (Phase timescale). (b) Average number of GMRES iterations per time step as a function of time step size. (c) Error as a function of CPU time.

To assess algorithmic performance of our method, we consider CPU time required for time integration to a fixed $t = t_f$ as a function of time step size (Δt). In this context, we define a method as ideally algorithmically scalable if CPU time required for time integration is inversely proportional to Δt . With this definition, explicit methods are inherently ideally algorithmically scalable. Figure 4a shows CPU time as a function of Δt for explicit Euler (EE), Crank-Nicolson (CN), and Crank-Nicolson with preconditioning (CN-PRE). Figure 4a confirms algorithmic scalability for EE for $\Delta t < \Delta t_T$ (the explicit CFL limit). Algorithmic scalability is also confirmed for (unpreconditioned) CN for $\Delta t < \Delta t_\varphi$; however for $\Delta t > \Delta t_\varphi$, the cost of the method increases. When effectively preconditioned, CN scales well algorithmically for Δt up to $4 \Delta t_\varphi$.

Recall that the dominant cost in JFNK is GMRES iterations, and the key idea for preconditioning is to reduce the number of GMRES iterations per nonlinear solve. Figure 4b demonstrates the effect of preconditioning and shows average number of GMRES iterations as a function of time step size. The average number of GMRES iterations remains constant for CN up to $\Delta t = \Delta t_\varphi$ and increases rapidly for $\Delta t > \Delta t_\varphi$. In contrast, the average number of GMRES iterations remains constant for CN-PRE up to $\Delta t = 4 \Delta t_\varphi$. Additionally, our preconditioning approach reduces the number of GMRES iterations at each Newton step by a factor of 2 to 3. As a well-conditioned, non-symmetric mass matrix must be approximately inverted each time step for EE, the average number of GMRES iterations per time step for EE is also shown in Fig. 4b.

Figure 4c shows error as a function of cost in terms of CPU time for EE, CN, and CN-PRE. Figure 4c shows EE to have less error, however costs considerably more than CN; and demonstrates that for a given level of accuracy, implicit methods can require less cost in terms of CPU time. Effective preconditioning allows the implicit method to scale algorithmically with larger time steps than explicit methods, while maintaining second-order temporal accuracy.

4.2. Directional growth

Similar to free growth, directional crystallization of alloys is also a well-understood benchmark problem but more relevant for additive manufacturing [1–4]. In this case, the evolution equations in Sec. 4.1 were modified to accommodate the evolving $u(\mathbf{x}, t)$ and $T(\mathbf{x}, t)$ fields. We model directional growth of a sample alloy in 2D and 3D following [80]. With a particular choice of $f(\varphi, u)$, Eq. (8) becomes

$$F_1(\varphi_h^{n+1}, u_h^{n+1})_i = \frac{1}{\Delta t} \left[\left([1 + (1-k)u_h^{n+1}] g_s^2(\vartheta^{n+1}) \varphi_h^{n+1}, \psi_i \right) - \left([1 + (1-k)u_h^n] g_s^2(\vartheta^n) \varphi_h^n, \psi_i \right) \right]$$

ϵ	Anisotropy	0.01	k	Equilibrium partition coefficient	0.14
m	Liquidus slope (K/wt%)	-2.6	c_∞	Alloy (Al-Cu) composition (wt%)	3
λ	Coupling constant	10.0	D	Liquid diffusivity (m ² /s)	3×10^{-9}
d_0	Capillary length (m)	5×10^{-9}	G	Thermal gradient (K/m)	10^4
Γ	Gibbs-Thomson coefficient (K m)	2.4×10^{-7}	R	Growth rate (m/s)	10^{-2}

Table 3

Material properties and simulation parameters in Eqs. (38)–(43), adopted from [82].

$$\begin{aligned}
& + \theta \left(g_s^2(\vartheta^{n+1}) \nabla \varphi_h^{n+1}, \nabla \psi_i \right) + (1 - \theta) \left(g_s^2(\vartheta^n) \nabla \varphi_h^n, \nabla \psi_i \right) \\
& + \theta \left(g_s(\vartheta^{n+1}) \|\nabla \varphi_h^{n+1}\|^2, \nabla \psi_i \right) + (1 - \theta) \left(g_s(\vartheta^n) \|\nabla \varphi_h^n\|^2, \nabla \psi_i \right) \\
& \quad - \theta \left(G_3(\varphi_h^{n+1})(u_h^{n+1} + G_4), \psi_i \right) - (1 - \theta) \left(G_3(\varphi_h^n)(u_h^n + G_4), \psi_i \right), \quad (38)
\end{aligned}$$

with

$$G_3(\varphi_h) = \varphi_h - \varphi_h^3 - \lambda(1 - \varphi_h^2)^2 \quad (39)$$

and

$$G_4(x, t) = \frac{G(x - Rt)}{|m|c_\infty(1 - k)/k}, \quad (40)$$

where x is the direction of thermal gradient or dendrite growth. Similarly, Eq. (9) for u becomes

$$\begin{aligned}
F_2(\varphi_h^{n+1}, u_h^{n+1})_i &= \frac{1}{\Delta t} \left[\left(\frac{1+k}{2} u_h^{n+1}, \psi_i \right) - \left(\frac{1+k}{2} u_h^n, \psi_i \right) \right] \\
& + \theta \left(\frac{1 - \varphi_h^{n+1}}{2} D \nabla u_h^{n+1}, \nabla \psi_i \right) + (1 - \theta) \left(\frac{1 - \varphi_h^n}{2} D \nabla u_h^n, \nabla \psi_i \right) \\
& \quad + \left(\mathbf{j}_{\text{at}}(\widehat{\varphi}_h^n), \nabla \psi_i \right) - \left(\frac{1}{2} \widehat{\varphi}_h^n [1 + (1 - k)u_h^{n+1}], \psi_i \right), \quad (41)
\end{aligned}$$

with $\widehat{\varphi}_h$ given by Eq. (11). We note that Eqs. (38)–(41) are nondimensional, where the constant λ in Eq. (39) characterizes the length scale of the interface $W = d_0\lambda/a_1$ and the time scale $\tau = (d_0^2/D)a_2\lambda^3$, with $a_1 = 0.8839$ and $a_2 = 0.6267$. The anti-trapping current,

$$\mathbf{j}_{\text{at}}(\widehat{\varphi}_h) = \frac{1}{2\sqrt{2}} [1 + (1 - k)u_h] \widehat{\varphi}_h \nabla \varphi_h, \quad (42)$$

avoids artificial interfacial effects on solute field [81]. The nondimensional concentration u is related to solute composition c (wt%) by

$$u = \frac{\left(\frac{2c k/c_\infty}{1+k-(1-k)\varphi} \right) - 1}{1 - k}. \quad (43)$$

Material properties and numerical parameters are listed in Table 3. We utilize 9 quadrature points in each quadrilateral element (2D) and 27 quadrature points in each hexahedral element (3D) to accurately integrate the nonlinear terms in Eqs. (38)–(41).

Simulations were performed on meshes consisting of 1024×256 (2D) and $1024 \times 256 \times 256$ (3D) elements with $h = 0.8$, implicit time integration with $\theta = 1$ and $\Delta t = 0.002$, and zero Neumann boundary conditions on $\partial\Omega$. Initial conditions consist of a solid-liquid interface at $x = 8$ units, with

$$\varphi(\mathbf{x}, 0) = \begin{cases} 1 & : 0 \leq x \leq 8 \\ -1 & : x > 8 \end{cases}, \quad (44)$$

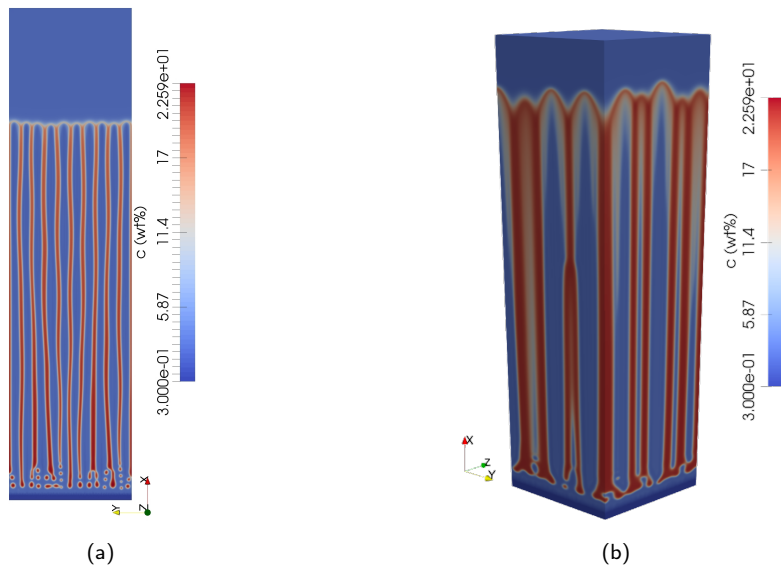


Figure 5: Alloy dendrite evolution using the phase-field model (Eqs. (38)–(41)) and physical properties (Table 3). (a) 2D simulation snapshot for dimensionless $t_f = 170$. The composition field (wt%) is shown at the steady-state. The dimensional solute redistribution profile is shown using a color bar. (b) The corresponding 3D simulation snapshot. The gradient or growth direction, x , is vertical in the figure.

where $\varphi = 1$ corresponds to solid and $\varphi = -1$ corresponds to liquid. The initial solute concentration $u(\mathbf{x}, 0) = -1$ corresponds to $c = k c_\infty$ in solid and $c = c_\infty$ in liquid. A small, random perturbation is applied to the initial solid-liquid interface.

The perturbation grows with time, starting with the transient stages of growth followed by steady-state, when the dendrite tips grow with constant velocity. The evolution of columnar dendritic microstructure is shown in 2D in Fig. 5a and the same is shown in 3D in Fig. 5b. The finger-like cellular features are colored by c . Simulations are essential to study materials behavior in applications, for example, the redistribution of c across, along, and through the cells determine the solute-trapping behavior of the alloy material [9, 82–84]. This can be easily explored in detail by varying G and R in our simulations using the Tusas framework; a study of which is beyond the scope of this work.

The 3D simulations were performed on Summit at Oak Ridge National Laboratory [85] across multiple GPUs and multiple nodes using MPI and CUDA. The 3D simulations demonstrate an advanced capability of Tusas to perform large-scale long-time simulations using next-generation parallel computing techniques; the details of our hybrid parallel implementation is given in Sec. 4.3.

4.3. Parallel performance

In addition to performing well in parallel across multiple CPUs using MPI and OpenMP, a particular strength of Tusas is the ability to run efficiently across multiple GPUs using MPI and CUDA. As the residual fill in Eqs. (38)–(41) is composed entirely of local operations, it is performed entirely on the GPU utilizing a distance-1 element graph coloring within each MPI subdomain. Element graph coloring avoids shared memory race conditions and atomic operations on CPU threads and GPUs. In addition, inner products within the GMRES solver are implemented on the GPU *via* the Belos and Kokkos packages in Trilinos [64].

To demonstrate strong and weak parallel multi-node and multi-GPU scaling, we consider simulations for the 3D problem discussed in Sec. 4.2 with discretizations consisting of 17,073,666,

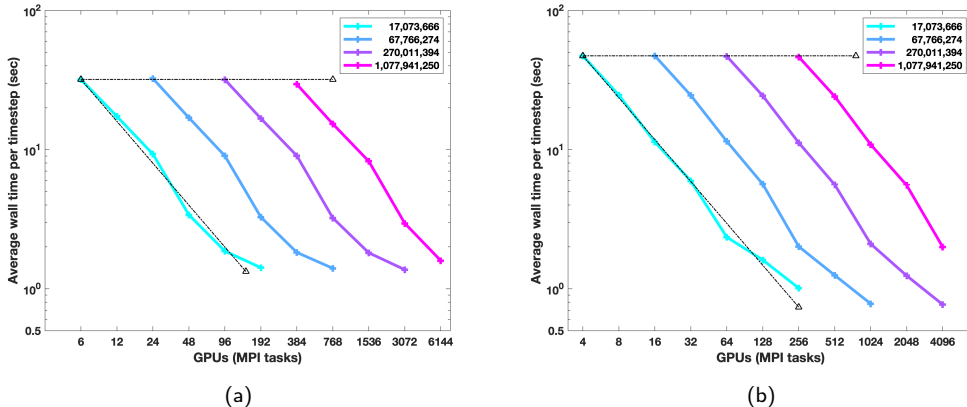


Figure 6: (a) Strong and weak multi-node, multi-GPU scaling on Summit. (b) Strong and weak multi-node, multi-GPU scaling on Sierra.

67,766,274, 270,011,394, and 1,077,941,250 unknowns. The discretizations consist of meshes with $512 \times 128 \times 128$, $512 \times 256 \times 256$, $512 \times 512 \times 512$, and $512 \times 1024 \times 1024$ bilinear hexahedral elements.

Scaling results were performed on Summit at Oak Ridge National Laboratory [85] and Sierra at Lawrence Livermore National Laboratory [86]. Summit is comprised of 4,608 nodes, each node consists of 2 IBM Power9 CPUs, 6 NVIDIA Volta V100 GPUs and 512 GB memory, and achieves 148.6 PetaFLOPS peak performance; Sierra is comprised of 4,320 nodes, each node consists of 2 IBM Power9 CPUs, 4 NVIDIA Volta V100 GPUs and 256 GB memory, and achieves 94.6 PetaFLOPS peak performance.

Strong scaling is defined by how CPU time varies with the number of processors for a fixed total problem size and is used to determine if the software is compute-bound. Ideal strong scaling is achieved if the CPU time is inversely proportional to the number of processing elements used. Weak scaling is defined by how CPU time varies with the number of processors for a fixed problem size per processor and is used to determine if the software is memory bound. Ideal weak scaling is achieved if the CPU time remains constant while the workload is increased in direct proportion to the number of processors.

Figure 6 shows the CPU time required for time integration to a fixed time as a function of the number of GPUs. Specifically, Fig. 6a shows strong and weak scaling on Summit on up to 6,144 GPUs (1,024 nodes), and Fig. 6b shows strong and weak scaling on Sierra on up to 4,096 GPUs (1,024 nodes). Strong scaling is depicted by solid lines on Fig. 6, where each color depicts a fixed problem size. Weak scaling is depicted by horizontal markers. This preliminary scaling study demonstrates that Tusas effectively scales strongly and weakly on thousands of GPUs with billions of unknowns and is particularly suited for emerging heterogeneous architectures. A detailed study of parallel implementation, performance, scalability, and efficiency is beyond the scope of this work and will be the focus of a separate manuscript.

5. Discussion and summary

We have presented an implicit approach for predictive phase-field simulation of solidification. The method is based on implicit time integration, where the solution of the nonlinear system is approx-

imated by JFNK with physics-based preconditioning. Spatial discretization consists of an unstructured, nodal finite element method. Such a combination of advanced, modern numerical approaches and preconditioning facilitates ideal algorithmic efficiency and scalability at time steps greater than that traditional CFL limits allow.

In this edition, we introduce a new open-source phase-field modeling framework, *Tusas*, and demonstrate its efficacy on phase-field simulations of dendritic solidification for pure and binary alloy materials assuming both isothermal and directional growth conditions. The framework is constructed using modern computational science and solver libraries and is implemented utilizing a hybrid parallel approach on modern heterogeneous architectures. We have demonstrated ideal strong and weak scaling on up to a billion unknowns and thousands of GPUs on Summit [85] and Sierra [86], currently the two fastest supercomputers in the world.

Currently, *Tusas* is playing a critical role in studying solidification of metals and alloys in engineering processes, in particular, additive manufacturing [3, 82], as we continue to prepare for exascale computing [87, 88]. In conclusion, we have shown that modern algorithms, discretizations, and computational science, and heterogeneous hardware provide a robust route for predictive phase-field simulation of microstructures that will complement experimental studies and provide significant contributions to better understanding material behavior rapidly.

Declaration of competing interest

The authors declare that they have no known competing financial interests or personal relationships that could have appeared to influence the work reported in this paper.

Acknowledgments

This work was supported by the U.S. Department of Energy through the Los Alamos National Laboratory. Los Alamos National Laboratory is operated by Triad National Security, LLC, for the National Nuclear Security Administration of U.S. Department of Energy (Contract No. 89233218CNA000001) and by the Exascale Computing Project (17-SC-20-SC), a joint project of the U.S. Department of Energy's Office of Science and National Nuclear Security Administration, responsible for delivering a capable exascale ecosystem, including software, applications, and hardware technology, to support the nation's exascale computing imperative (LA-UR-20-23977).

References

- [1] M. Rappaz, J. A. Dantzig, *Solidification*, Engineering sciences, EPFL Press, Lausanne, 2009.
- [2] W. Kurz, D. J. Fisher, *Fundamentals of Solidification*, Trans Tech Publications, Zurich, 1998.
- [3] M. M. Francois, A. Sun, W. E. King, N. J. Henson, D. Tourret, C. A. Bronkhorst, N. N. Carlson, C. K. Newman, T. S. Haut, J. Bakosi, et al., Modeling of additive manufacturing processes for metals: Challenges and opportunities, *Current Opinion in Solid State and Materials Science* 21 (2017).
- [4] S. Ghosh, Predictive modeling of solidification during laser additive manufacturing of nickel superalloys: recent developments, future directions, *Materials Research Express* 5 (2018) 012001.
- [5] T. Keller, G. Lindwall, S. Ghosh, L. Ma, B. Lane, F. Zhang, U. R. Kattner, E. A. Lass, J. C. Heigel, Y. Idell, M. E. Williams, A. J. Allen, J. E. Guyer, L. E. Levine, Application of Finite Element, Phase-field, and CALPHAD-based Methods to Additive Manufacturing of Ni-based Superalloys, *Acta Materialia* 139 (2017) 244–253.
- [6] Y. Ji, L. Chen, L.-Q. Chen, Understanding microstructure evolution during additive manufacturing of metallic alloys using phase-field modeling, in: *Thermo-Mechanical Modeling of Additive Manufacturing*, Elsevier, NY, 2018, pp. 93–116.
- [7] R. Acharya, J. A. Sharon, A. Staroselsky, Prediction of microstructure in laser powder bed fusion process, *Acta Materialia* 124 (2017) 360–371.
- [8] J. Kundin, L. Mushongera, H. Emmerich, Phase-field modeling of microstructure formation during rapid solidification in Inconel 718 superalloy, *Acta Materialia* 95 (2015) 343 – 356.
- [9] S. Ghosh, L. Ma, N. Ofori-Opoku, J. E. Guyer, On the primary spacing and microsegregation of cellular dendrites in laser deposited Ni-Nb alloys, *Model. Simul. Mater. Sci. Eng.* 25 (2017) 065002.

- [10] S. Ghosh, L. Ma, L. E. Levine, R. E. Ricker, M. R. Stoudt, J. C. Heigel, J. E. Guyer, Single-track melt-pool measurements and microstructures in Inconel 625, *JOM* (2018) 1–6.
- [11] S. Ghosh, K. McReynolds, J. E. Guyer, D. Banerjee, Simulation of temperature, stress and microstructure fields during laser deposition of Ti–6Al–4V, *Model. Simul. Mater. Sci. Eng.* 26 (2018) 075005.
- [12] K. Karayagiz, L. Johnson, R. Seede, V. Attari, B. Zhang, X. Huang, S. Ghosh, T. Duong, I. Karaman, A. Elwany, R. Arroyave, Finite interface dissipation phase field modeling of Ni–Nb under additive manufacturing conditions, *Acta Materialia* 185 (2020) 320–339.
- [13] L. Q. Chen, Phase-field models for microstructure evolution, *Annu. Rev. Mater. Res.* 32 (2002) 113–140.
- [14] W. J. Boettinger, J. A. Warren, C. Beckermann, A. Karma, Phase-field simulation of solidification, *Annu. Rev. Mater. Res.* 32 (2002) 163–194.
- [15] N. Moelans, B. Blanpain, P. Wollants, An introduction to phase-field modeling of microstructure evolution, *Calphad* 32 (2008) 268 – 294.
- [16] I. Steinbach, Phase-field models in materials science, *Modelling Simul. Mater. Sci. Eng.* 17 (2009) 073001.
- [17] J. Lambert, Numerical methods for ordinary differential systems: The initial value problem, John Wiley & Sons, Hoboken, NJ, 1991.
- [18] S. Brenner, R. Scott, The mathematical theory of finite element methods, volume 15, Springer Science & Business Media, New York, 2007.
- [19] D. Braess, Finite Elements: Theory, Fast Solvers, and Applications in Solid Mechanics, Cambridge University Press, Cambridge, 2001.
- [20] D. A. Knoll, D. E. Keyes, Jacobian-free Newton-Krylov methods: a survey of approaches and applications, *J. Comput. Phys.* 193 (2004) 357–397.
- [21] C. T. Kelley, Iterative Methods for Linear and Nonlinear Equations, SIAM, Philadelphia, PA, 1995.
- [22] D. A. Knoll, W. J. Rider, A multigrid preconditioned Newton-Krylov method, *SIAM J. Sci. Comput.* 21 (2000) 691–710.
- [23] Y. Saad, Iterative Methods for Sparse Linear Systems, The PWS Series in Computer Science, PWS Publishing Company, Boston, MA, 1995.
- [24] W. Gropp, E. Lusk, A. Skjellum, Using MPI: portable parallel programming with the message-passing interface, volume 1, MIT press, 1999.
- [25] L. Dagum, R. Menon, OpenMP: An industry-standard API for shared-memory programming, *IEEE Comput. Sci. Eng.* 5 (1998) 46–55.
- [26] NVIDIA Corporation, NVIDIA CUDA C programming guide, 2010. Version 3.2.
- [27] D. Jacobsen, J. Thibault, I. Senocak, An MPI-CUDA implementation for massively parallel incompressible flow computations on multi-GPU clusters, in: 48th AIAA Aerospace Sciences Meeting Including the New Horizons Forum and Aerospace Exposition, p. 522.
- [28] J. Glaser, T. D. Nguyen, J. A. Anderson, P. Lui, F. Spiga, J. A. Millan, D. C. Morse, S. C. Glotzer, Strong scaling of general-purpose molecular dynamics simulations on GPUs, *Computer Physics Communications* 192 (2015) 97–107.
- [29] D. Komatitsch, G. Erlebacher, D. Göddeke, D. Michéa, High-order finite-element seismic wave propagation modeling with MPI on a large GPU cluster, *J. Comput. Phys.* 229 (2010) 7692–7714.
- [30] D. Gaston, C. Newman, G. Hansen, D. Lebrun-Grandie, MOOSE: A parallel computational framework for coupled systems of nonlinear equations, *Nuclear Engineering and Design* 239 (2009) 1768–1778.
- [31] PACE3D (Parallel Algorithms for Crystal Evolution in 3D), <https://www.hs-karlsruhe.de/en/research/hska-research-institutions/institute-for-digital-materials-science-idm/pace-3d-software/>, 2019.
- [32] MMSP (The Mesoscale Microstructure Simulation Project), <https://github.com/mesoscale/mmsp>, 2014.
- [33] MICRESS (The Microstructure Evolution Simulation Software), <https://micress.rwth-aachen.de/>, 2019.
- [34] OpenPhase, <http://www.openphase.de/>, 2007.
- [35] PhasePot Microstructure Simulation Tool, <https://phasepot.com/>, 2019.
- [36] J. E. Guyer, D. Wheeler, J. A. Warren, FiPy: Partial differential equations with Python, *Computing in Science & Engineering* 11 (2009) 6–15.
- [37] S. DeWitt, S. Rudraraju, D. Montiel, W. B. Andrews, K. Thornton, PRISMS-PF: A general framework for phase-field modeling with a matrix-free finite element method, *npj Computational Materials* 6 (2020).
- [38] M. R. Dorr, J.-L. Fattebert, M. Wickert, J. Belak, P. Turchi, A numerical algorithm for the solution of a phase-field model of polycrystalline materials, *J. Comput. Phys.* 229 (2010) 626–641.
- [39] B. Radhakrishnan, S. B. Gorti, J. A. Turner, R. Acharya, J. A. Sharon, A. Staroselsky, T. El-Wardany, Phase field simulations of microstructure evolution in IN718 using a surrogate Ni–Fe–Nb alloy during laser powder bed fusion, *Metals* 9 (2019) 14.
- [40] C. Zhu, J. Liu, M. Zhu, L. Feng, Multi-GPU hybrid programming accelerated three-dimensional phase-field model in binary alloy, *AIP Advances* 8 (2018) 035312.
- [41] A. Yamanaka, T. Aoki, S. Ogawa, T. Takaki, GPU-accelerated phase-field simulation of dendritic solidification in a

- binary alloy, *Journal of Crystal Growth* 318 (2011) 40–45.
- [42] T. Shimokawabe, T. Aoki, T. Takaki, T. Endo, A. Yamanaka, N. Maruyama, A. Nukada, S. Matsuoka, Peta-scale phase-field simulation for dendritic solidification on the TSUBAME 2.0 supercomputer, in: *Proceedings of 2011 International Conference for High Performance Computing, Networking, Storage and Analysis*, ACM, p. 3.
- [43] G. Caginalp, Stefan and Hele-Shaw type models as asymptotic limits of the phase-field equations, *Physical Review A* 39 (1989) 5887.
- [44] R. F. Sekerka, Morphology: from sharp interface to phase field models, *Journal of crystal growth* 264 (2004) 530–540.
- [45] G. B. Arfken, H. J. Weber, F. E. Harris, *Mathematical methods for physicists*, Elsevier, New York, 2013.
- [46] G. M. Ewing, *Calculus of variations with applications*, W. W. Norton and Co. Inc., New York, 1969.
- [47] S. M. Allen, J. W. Cahn, A microscopic theory for antiphase boundary motion and its application to antiphase domain coarsening, *Acta Metallurgica* 27 (1979) 1085 – 1095.
- [48] J. W. Cahn, J. E. Hilliard, Free energy of a nonuniform system. I. Interfacial free energy, *The Journal of chemical physics* 28 (1958) 258–267.
- [49] J. E. Dennis Jr, R. B. Schnabel, *Numerical methods for unconstrained optimization and nonlinear equations*, SIAM, Philadelphia, PA, 1996.
- [50] R. P. Pawlowski, J. N. Shadid, J. P. Simonis, H. F. Walker, Globalization techniques for Newton-Krylov methods and applications to the fully coupled solution of the Navier-Stokes equations, *SIAM Rev.* 48 (2006) 700–721.
- [51] M. Pernice, H. F. Walker, NITSOL: A Newton iterative solver for nonlinear systems, *SIAM J. Sci. Comp.* 19 (1998) 302–318.
- [52] P. N. Brown, Y. Saad, Hybrid Krylov methods for nonlinear systems of equations, *SIAM J. Sci. Statist. Comput.* 11 (1990) 450–481.
- [53] R. Dembo, S. C. Eisenstat, T. Steihaug, Inexact Newton methods, *SIAM J. Numer. Anal.* 19 (1982) 400–408.
- [54] S. C. Eisenstat, H. F. Walker, Choosing the forcing terms in an inexact Newton method, *SIAM J. Sci. Comput.* 17 (1996) 16–32.
- [55] L. Chacón, D. A. Knoll, J. M. Finn, An implicit, nonlinear reduced resistive MHD solver, *J. Comput. Phys.* 178 (2002) 15–36.
- [56] N. Provatas, K. Elder, *Phase-field methods in materials science and engineering*, John Wiley & Sons, Hoboken, NJ, 2011.
- [57] W. L. Briggs, S. F. McCormick, et al., *A multigrid tutorial*, volume 72, SIAM, Philadelphia, PA, 2000.
- [58] W. Hackbusch, *Multi-grid methods and applications*, volume 4, Springer Science & Business Media, New York, 2013.
- [59] U. Trottenberg, C. W. Oosterlee, A. Schüller, *Multigrid*, Academic Press, New York, 2000.
- [60] M. Gee, C. Siefert, J. Hu, R. Tuminaro, M. Sala, *ML 5.0 Smoothed Aggregation User’s Guide*, Technical Report SAND2006-2649, Sandia National Laboratories, 2006.
- [61] L. Berger-Vergiat, C. A. Glusa, J. J. Hu, M. Mayr, A. Prokopenko, C. M. Siefert, R. S. Tuminaro, T. A. Wiesner, *MueLu User’s Guide*, Technical Report SAND2019-0537, Sandia National Laboratories, 2019.
- [62] L. Berger-Vergiat, C. A. Glusa, J. J. Hu, M. Mayr, A. Prokopenko, C. M. Siefert, R. S. Tuminaro, T. A. Wiesner, *MueLu multigrid framework*, <http://trilinos.org/packages/muelu>, 2019.
- [63] M. A. Heroux, et al., An overview of the Trilinos project, *ACM Trans. Math. Softw.* 31 (2005) 397–423.
- [64] Trilinos, <https://github.com/trilinos/Trilinos>, 2019.
- [65] Exodus II, 2007. <http://sourceforge.net/projects/exodusii>.
- [66] L. Schoof, V. Yarberr, EXODUS II: A Finite Element Data Model, Technical Report SAND92-2137, Sandia National Laboratories, 1996.
- [67] NOX & LOCA: Object-Oriented Nonlinear Solver and Continuation Packages, <https://docs.trilinos.org/dev/packages/nox/doc/html/index.html>, 2010.
- [68] E. Bavier, M. Hoemmen, S. Rajamanickam, H. Thornquist, Amesos2 and Belos: Direct and iterative solvers for large sparse linear systems, *Scientific Programming* 20 (2012) 241–255.
- [69] M. A. Heroux, *AztecOO user guide*.
- [70] CMake, <https://cmake.org/>, 2019.
- [71] Boost C++ Libraries, <http://www.boost.org/>, 2019.
- [72] The HDF Group, *Hierarchical Data Format*, version 5, 1997. <http://www.hdfgroup.org/HDF5/>.
- [73] R. Rew, G. Davis, Data management: NetCDF: An interface for scientific data access, *IEEE Comput. Graph. Appl.* 10 (1990) 76–82.
- [74] Kokkos C++ Performance Portability Programming EcoSystem: The Programming Model - Parallel Execution and Memory Abstraction, <https://github.com/kokkos/kokkos>, 2020.
- [75] H. C. Edwards, C. R. Trott, D. Sunderland, Kokkos: Enabling manycore performance portability through polymorphic memory access patterns, *Journal of Parallel and Distributed Computing* 74 (2014) 3202 – 3216.
- [76] Tusas, <https://github.com/chrisknewman/tusas>, 2020.
- [77] A. M. Jokisaari, P. W. Voorhees, J. E. Guyer, J. A. Warren, O. G. Heinonen, Phase field benchmark problems for dendritic growth and linear elasticity, *Computational Materials Science* 149 (2018) 336–347.

- [78] S. J. Cummins, J. J. Quirk, D. B. Kothe, An exploration of the phase field technique for microstructure solidification modeling, in: Proceedings of IMECE 2002 ASME Microstructural Developments in Solidification, ASME, New Orleans, 2002.
- [79] D. A. Kessler, H. Levine, Velocity selection in dendritic growth, *Physical Review B* 33 (1986) 7867.
- [80] B. Echebarria, R. Folch, A. Karma, M. Plapp, Quantitative phase-field model of alloy solidification, *Phys. Rev. E* 70 (2004) 061604.
- [81] A. Karma, Phase-field formulation for quantitative modeling of alloy solidification, *Phys. Rev. Lett.* 87 (2001) 115701.
- [82] A. Farzadi, M. Do-Quang, S. Serajzadeh, A. Kokabi, G. Amberg, Phase-field simulation of weld solidification microstructure in an Al–Cu alloy, *Modelling Simul. Mater. Sci. Eng.* 16 (2008) 1–18.
- [83] S. Ghosh, N. Ofori-Opoku, J. E. Guyer, Simulation and analysis of γ -Ni cellular growth during laser powder deposition of Ni-based superalloys, *Computational Materials Science* 144 (2018) 256–264.
- [84] S. Ghosh, M. R. Stoudt, L. E. Levine, J. E. Guyer, Formation of Nb-rich droplets in laser deposited Ni-matrix microstructures, *Scripta Materialia* 146 (2018) 36–40.
- [85] Summit, <https://www.olcf.ornl.gov/olcf-resources/compute-systems/summit/>, 2018.
- [86] Sierra, <https://computing.llnl.gov/computers/sierra/>, 2018.
- [87] D. Kothe, S. Lee, I. Qualters, Exascale computing in the United States, *Comput. Sci. Eng.* 21 (2018) 17–29.
- [88] F. Alexander, et al., Exascale applications: skin in the game, *Philos. Trans. R. Soc. A* 378 (2020).